СТРОИТЕЛЬНАЯ МЕХАНИКА ИНЖЕНЕРНЫХ КОНСТРУКЦИЙ И СООРУЖЕНИЙ
STRUCTURAL MECHANICS OF ENGINEERING CONSTRUCTIONS AND BUILDINGS

2025. 21(5). 441–461

ISSN 1815-5235 (Print), 2587-8700 (Online)

HTTP://JOURNALS.RUDN.RU/STRUCTURAL-MECHANICS

DOI: 10.22363/1815-5235-2025-21-5-441-461
EDN: DEEXQA

Research article / Научная статья

Triangular Layered Finite Element Method for Reinforced Concrete Slabs

Dara A. Mawlood✉, **Alexandr A. Koyankin**

Siberian Federal University, *Krasnoyarsk, Russian Federation*
✉ dara.mawloud@univsul.edu.iq

Received: August 3, 2025
Revised: October 4, 2025
Accepted: October 14, 2025

Abstract. This study presents an advanced layered triangular finite element method for modeling reinforced concrete (RC) slabs, incorporating material nonlinearity based on a refined global-local plate theory. The RC slab's cross-section is discretized into concrete and steel layers, each modeled as an individual plate element with distinct material properties. The proposed formulation independently considers displacement field variables and out-of-plane stress components, enabling precise nodal stress determination through constitutive relationships. A three-node triangular element maintaining C1-continuity is employed for spatial discretization, with governing equations derived using a triangular layered plate theory. Benchmark verification studies confirm the method's computational accuracy and efficiency, with ultimate deflection predictions exhibiting errors ranging from 2.59% (minimum) to 11.2% (maximum). Comprehensive numerical tests demonstrate that the proposed triangular layered finite element approach delivers high-precision solutions while significantly reducing computational expense.

Keywords: kinematic layer, strain field, stress field, layered FE discretization, numerical results

Conflicts of interest. The authors declare that there is no conflict of interest.

Authors' contribution: *Mawlood D.A.* — data collection and processing, analysis and interpretation of results, scientific writing; *Koyankin A.A.* — concept development, approval of the final version of the manuscript. Both of the authors read and approved the final version of the article.

For citation: Mawlood D.A., Koyankin A.A. Triangular-layered finite element method for reinforced concrete slabs. *Structural Mechanics of Engineering Constructions and Buildings.* 2025;21(5):441–461. http://doi.org/10.22363/1815-5235-2025-21-5-441-461 EDN: DEEXQA

Метод многослойных треугольных конечных элементов для железобетонных плит перекрытия

Д.А. Мавлуд✉, **А.А. Коянкин**

Сибирский федеральный университет, *Красноярск, Российская Федерация*
✉ dara.mawloud@univsul.edu.iq

Поступила в редакцию: 3 августа 2025 г.
Доработана: 4 октября 2025 г.
Принята к публикации: 14 октября 2025 г.

Аннотация. Представлен усовершенствованный многослойный треугольный метод конечных элементов для моделирования железобетонных плит, учитывающий нелинейность материала на основе усовершенствованной глобально-локальной теории пластин. Поперечное сечение железобетонной плиты разбито на бетонные и стальные слои, представ-

Dara A. Mawlood, Master student, Department of Building Structures and Controlled Systems, Institute of Civil Engineering, Siberian Federal University, 79 Svobodny av., 660041, Krasnoyarsk, Russian Federation; ORCID: 0009-0003-2819-3107; e-mail: dara.mawloud@univsul.edu.iq

Alexandr A. Koyankin, Candidate of Technical Sciences, Associate Professor of the Department of Building Structures and Controlled Systems, Institute of Civil Engineering, Siberian Federal University, 79 Svobodny av., 660041, Krasnoyarsk, Russian Federation; eLIBRARY SPIN-code: 2779-8314, ORCID: 0000-0001-5271-9904; e-mail: KoyankinAA@mail.ru

ляющие собой отдельные элементы с различными свойствами материала. Предлагаемая формулировка независимо учитывает переменные поля смещений и компоненты напряжений вне плоскости, что позволяет точно устанавливать узловое напряжение с помощью определяющих соотношений. Для пространственной дискретизации используется треугольный элемент с тремя узлами, поддерживающий непрерывность порядка C1, а основные уравнения получены с использованием теории многослойных треугольных пластин. Сравнительные проверочные исследования подтвердили точность вычислений и эффективность метода, при этом погрешность результатов расчета прогиба составляет от 2,59 % (минимум) до 11,2 % (максимум). Всесторонние численные эксперименты демонстрируют, что предложенный метод многослойных треугольных конечных элементов обеспечивает высокую точность решений при значительном снижении вычислительных затрат.

Ключевые слова: кинематический слой, поле деформаций, поле напряжений, разбиение на многослойные КЭ, численные результаты

Заявление о конфликте интересов. Авторы заявляют об отсутствии конфликта интересов.

Вклад авторов: *Мавлуд Д.А.* — сбор и обработка материалов, анализ и интерпретация данных, подготовка и редактирование текста; *Коянкин А.А.* — разработка концепции, утверждение окончательного варианта статьи. Оба автора ознакомлены с окончательной версией статьи и одобрили ее.

Для цитирования: *Mawlood D.A., Koyankin A.A.* Triangular layered finite element method for reinforced concrete slabs // Строительная механика инженерных конструкций и сооружений. 2025. Т. 21. № 5. С. 441–461. http://doi.org/10.22363/1815-5235-2025-21-5-441-461 EDN: DEEXQA

1. Introduction

From the 2010–2025 construction period, reinforced concrete (RC) slabs are essential structural components, serving as flooring systems while carrying vertical loads. Accurate performance analysis is critical to ensure both safety and cost-effectiveness in RC building designs [1; 2]. However, predicting the nonlinear response of RC slabs remains a significant challenge due to the complex behavior of reinforced concrete structures, making it an active research area [3; 4]. This complexity arises from material nonlinearity in concrete and steel, cracking, imperfect bond-slip behavior, and time-dependent effects such as creep and shrinkage [5].

Several material models have been developed to capture the layered nonlinear behavior of RC slabs. For reinforcing steel, a uniaxial elastic-plastic stress-strain relationship is typically employed, exhibiting symmetrical response under both tension and compression. Similarly, concrete behavior can be effectively represented using a bilinear stress-strain approximation that incorporates tensile capacity [5; 6].

To address the limitations of conventional 3D finite element models, researchers have developed innovative layered methods [7; 8]. Unlike simplified effective stiffness approaches, these layered FE models enable precise prediction of ultimate bending and shear capacity in RC slabs [9; 10]. The methods employ triangular plate elements composed of perfectly bonded, superimposed equivalent layers representing both concrete and steel reinforcement. This layered triangular element facilitates detailed tracking of concrete failure mechanisms (including cracking and crushing) and progressive steel yielding throughout the slab depth [11; 12]. Although numerous layer-based FE models exist for RC slab analysis, current implementations remain predominantly limited by Kirchhoff-Thin Plate Theory (KTPT) assumptions [13; 14].

Current research indicates a strong preference for displacement-based formulations in finite element modeling of RC slabs and plate structures [15; 16]. While these layered triangular elements derive stress components indirectly through numerical differentiation of displacement fields, the resulting post-processed stresses particularly out-of-plane components, often demonstrate reduced accuracy compared to their displacement counterparts. In contrast, advanced layered FE formulations for composite structures treat stresses and displacements as independent variables, thereby achieving superior stress prediction accuracy [17; 18].

Although layered finite element formulations have been widely adopted for laminated composite analysis, their application to nonlinear RC slab modeling remains relatively limited. Recent advances by Liguori et al. [19; 20] introduced a mixed finite element formulation for nonlinear material analysis of RC shell structures. These layered triangular elements utilize conventional Mindlin-Reissner plate theory to describe displacement fields in

Мавлуд Дара, магистрант кафедры строительных конструкций и управляемых систем, Инженерно-строительный институт, Сибирский федеральный университет, Российская Федерация, 660041, г. Красноярск, пр. Свободный, д. 79; ORCID: 0009-0003-2819-3107; e-mail: dara.mawloud@univsul.edu.iq

Коянкин Александр Александрович, кандидат технических наук, доцент кафедры строительных конструкций и управляемых систем, Инженерно-строительный институт, Сибирский федеральный университет, Российская Федерация, 660041, г. Красноярск, пр. Свободный, д. 79; eLIBRARY SPIN-код: 2779-8314, ORCID: 0000-0001-5271-9904; e-mail: KoyankinAA@mail.ru

RC structural analysis. In contrast to their methods the present study implements an innovative global-local kinematic framework for displacement field representation in plate analysis. Notably, while Liguori et al. [20] treated both membrane/flexural stresses and displacement fields as primary unknowns in their formulation, the current approach adopts a distinct strategy for variable selection. Wang et al. proposed an efficient quasi-three-dimensional mixed finite element formulation based on a refined layered global-local plate theory for nonlinear analysis of RC slabs. In this approach, the cross-section is discretized into distinct concrete and steel layers, with each layer modeled as an independent plate element characterized by unique material properties [21].

This study introduces an innovative computational framework for nonlinear analysis of RC slabs, based on an advanced triangular-layered global-local plate theory formulation. The proposed triangular layered plate methods offer optimal computational advantages, combining superior geometric flexibility with adaptive finite element analysis capabilities for RC slab modeling. The framework employs a 3-node triangular composite plate element augmented with additional nodal degrees of freedom to explicitly represent out-of-plane stress components. While requiring additional field variables, this approach enables direct computation of through-thickness stress distributions during nonlinear solution procedures.

The formulation is derived through a parameterized mixed variational principle, providing rigorous mathematical foundations for the methods The RC slab is modeled as an assembly of perfectly bonded concrete and steel layers, with material nonlinearities addressed through: (1) a smeared crack formulation for concrete behavior, and (2) elasto-plastic theory for steel reinforcement response.

2. Methods

For reinforced concrete slab elements, the principles of membrane and plate bending theory **exist**, as will be demonstrated in the subsequent steps.

2.1. Membrane Element Analysis

For the membrane component, a standard 3-node triangular element is defined by its node numbering and their (*x, y*) coordinates. (Figures 1 and 2) [6; 13].

$$u = N_1 u_1 + N_2 u_2 + N_3 u_3,$$
$$v = N_1 v_1 + N_2 v_2 + N_3 v_3 \tag{1}$$

where (u_i, v_i) represent the horizontal and vertical displacements at node *i*, and N_i denotes the corresponding shape function for that node.

The shape functions for the 3-noded triangular element are derived as follows:

$$u = \alpha_1 + \alpha_2 x + \alpha_3 y,$$
$$v = \beta_1 + \beta_2 x + \beta_3 y. \tag{2}$$

The system was solved for coefficients, and substituting these solutions back into Equation (2) produces:

$$u = 1/\left(2A^{(e)}\right)\left[\left(a_1 + b_1 x + c_1 y\right)u_1 + \left(a_2 + b_2 x + c_2 y\right)u_2 + \left(a_3 + b_3 x + c_3 y\right)u_3\right],$$

where $A^{(e)}$ is the element area and,

$$i, j \;\; a_i = x_j y_k - x_k y_j,\; b_i = y_j - y_k,\; c_i = x_k - x_j \qquad i, j, k = 1, 2, 3.$$

The coefficients $a_i, b_i,$ and c_i are determined through cyclic permutation of the indices (i, j, k). A comparison of Equation (2) with Equation (1) yields the explicit expressions for the shape functions:

$$N_i = 1/\left(2A^{(e)}\right)\left(a_i + b_i x + c_i y\right) \qquad i = 1, 2, 3. \tag{3}$$

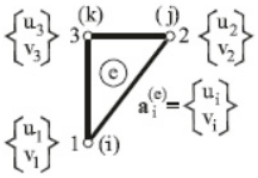

Figure 1. Discretization of a structure into 3-noded triangular elements
S o u r c e: made by H. Werkle [6].

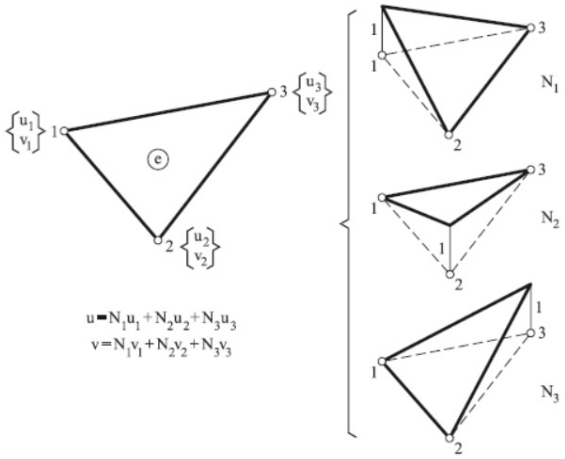

Figure 2. Shape functions for the 3-noded triangular element
S o u r c e: made by E. Oñate [13].

2.1.1. Membrane-Induced Strain

The strain components (ε_x, ε_y, γ_{xy}) are computed via differentiation of the displacement fields *u(x,y)* and *v(x,y)* represented by their respective shape functions:

$$\begin{pmatrix} \varepsilon_x \\ \varepsilon_y \\ \gamma_{xy} \end{pmatrix} = \begin{pmatrix} \dfrac{\partial u}{\partial x} \\ \dfrac{\partial v}{\partial y} \\ \dfrac{\partial u}{\partial y} + \dfrac{\partial v}{\partial x} \end{pmatrix} = \begin{bmatrix} \dfrac{\partial N1}{\partial x} & 0 & \dfrac{\partial N2}{\partial x} & 0 & \dfrac{\partial N3}{\partial x} & 0 \\ 0 & \dfrac{\partial N1}{\partial y} & 0 & \dfrac{\partial N2}{\partial y} & 0 & \dfrac{\partial N3}{\partial y} \\ \dfrac{\partial N1}{\partial y} & \dfrac{\partial N1}{\partial x} & \dfrac{\partial N2}{\partial y} & \dfrac{\partial N2}{\partial x} & \dfrac{\partial N3}{\partial y} & \dfrac{\partial N3}{\partial x} \end{bmatrix} \begin{bmatrix} u_1 \\ v_1 \\ u_2 \\ v_2 \\ u_3 \\ v_3 \end{bmatrix}, \tag{4}$$

$$\varepsilon_m = \beta_m . u_e, \tag{5}$$

where

$$B_{mi} = \frac{1}{2A^e} \begin{bmatrix} b_i & 0 \\ 0 & c_i \\ c_i & b_i \end{bmatrix}.$$

2.1.2. Membrane-Induced Stress

The stresses in the element are calculated from the strains by applying Hooke's law, as shown in [11; 12]:

$$\begin{bmatrix} \sigma_x \\ \sigma_y \\ \tau_{xy} \end{bmatrix} = \frac{E}{1-\mu^2} \begin{bmatrix} 1 & \mu & 0 \\ \mu & 1 & 0 \\ 0 & 0 & \dfrac{1-\mu}{2} \end{bmatrix} \begin{bmatrix} \varepsilon_x \\ \varepsilon_y \\ \gamma_{xy} \end{bmatrix} \quad \text{or} \quad \sigma_m = D_m \varepsilon_m,$$

$$\sigma_m = D_m B_m u_e$$

and with the strains defined in (eq. 5), as:

$$\mathrm{s}_m = D_m B_m u_e, \tag{6}$$

where

$$D_m = \begin{bmatrix} d_{11} & d_{12} & 0 \\ d_{21} & d_{22} & 0 \\ 0 & 0 & d_{33} \end{bmatrix} = \frac{E}{1-\mu^2}\begin{bmatrix} 1 & \mu & 0 \\ \mu & 1 & 0 \\ 0 & 0 & \dfrac{1-\mu}{2} \end{bmatrix}.$$

These stresses are also referred to as membrane stresses [13].

2.1.3. Membrane Stiffness Formulation

Based on the stresses obtained from Equation (6), which were derived from displacement shape functions, the equivalent nodal forces are calculated using the principle of virtual displacements. The element stiffness submatrix $K_{ij}^{(e)}$, representing the interaction between nodes i and j within the element, is typically calculated as:

$$K_e^m = \int t B_m^T D_m B_m dx dy \tag{7}$$

substituting Equation (5) and (6) into Equation (7), yields:

$$K_{ij(e)}^m = \iint_{A^{(e)}} \frac{1}{2A^{(e)}}\begin{bmatrix} b_i & 0 & c_i \\ 0 & c_i & b_i \end{bmatrix}\begin{bmatrix} d_{11} & d_{12} & 0 \\ d_{21} & d_{22} & 0 \\ 0 & 0 & d_{33} \end{bmatrix}\frac{1}{2A^{(e)}}\begin{bmatrix} b_i & 0 \\ 0 & c_j \\ c_j & b_j \end{bmatrix} t\, dA.$$

For a homogeneous material, the integrand in Equation (8) remains constant, leading to:

$$K_{ij(e)}^{(m)} = \left(\frac{t}{4A}\right)^{(e)}\begin{bmatrix} b_i b_j d_{11} + c_i c_j d_{33} & b_i c_j d_{12} + b_j c_i d_{33} \\ c_i b_j d_{21} + b_i c_j d_{33} & b_i b_j d_{33} + c_i c_j d_{22} \end{bmatrix}. \tag{8}$$

2.2. Component for Bending

The Reissner — Mindlin plate theory is an advanced plate theory that incorporates shear deformation effects. This theory is commonly preferred for formulating finite plate elements. Plate deformations are described by the vertical displacement (w) and the rotational angles (φ_x, φ_y) at each point on the plate. Consequently, every node in the plate element possesses three degrees of freedom: one translational displacement (w_i) and two rotational components (φ_x, φ_y). The corresponding nodal forces consist of a transverse force (F_{zi}) and two bending moments (M_{xi}, M_{yi}). Figures 3, *a, b* show that, this 3-node element possesses nine degrees of freedom in total. The shape functions of a 3-node triangular element are constructed through bilinear interpolation of the nodal variables [6; 12].

$$w(x,y) = \alpha_1 + \alpha_2 x + \alpha_3 y + \alpha_4 x^2 + \alpha_5 xy + \alpha_6 y^2 + \alpha_7 x^3 + \alpha_8 x^2 y + \alpha_9 x y^2, \tag{9}$$

where

$$\varphi_x = \frac{\partial w}{\partial y}, \quad \text{and} \quad \varphi_y = \frac{\partial w}{\partial x}.$$

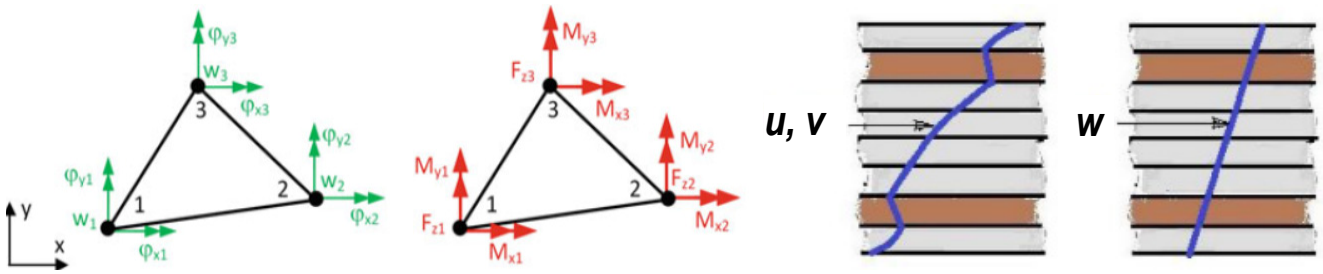

a *b* *1* *2*

S o u r c e: made by E. Oñate [13]. S o u r c e: made by R.Wang [21].

Figure 3. 3-node triangular element:
a — Triangular plate elements; *b* — Graphical illustration of the displacement field:
1 — in plane components, *2* — transverse component

$$\begin{bmatrix} w \\ \varphi_x \\ \varphi_y \end{bmatrix} = \begin{bmatrix} N_1 & 0 & 0 & N_2 & 0 & 0 & N_3 & 0 & 0 \\ 0 & N_1 & 0 & 0 & N_2 & 0 & 0 & N_3 & 0 \\ 0 & 0 & N_1 & 0 & 0 & N_2 & 0 & 0 & N_3 \end{bmatrix} \begin{bmatrix} w_1 \\ \varphi_{x1} \\ \varphi_{y1} \\ w_2 \\ \varphi_{x2} \\ \varphi_{y2} \\ w_3 \\ \varphi_{x3} \\ \varphi_{y3} \end{bmatrix}; \quad (10)$$

$u = N \cdot u_e$ N are denoted as *shape function.*

2.2.1. Bending Strain Components

The strain state of a plate element is determined by its curvature components and transverse shear deformations [5; 6]:

$$\begin{bmatrix} k_x \\ k_y \\ k_{xy} \end{bmatrix} = \begin{bmatrix} \dfrac{\partial \varphi_{xi}}{\partial x} \\ \dfrac{\partial \varphi_{yi}}{\partial y} \\ \dfrac{\partial \varphi_{xi}}{\partial y} + \dfrac{\partial \varphi_{yi}}{\partial x} \end{bmatrix} = \begin{bmatrix} 0 & \dfrac{\partial N_1}{\partial x} & 0 & 0 & \dfrac{\partial N_2}{\partial x} & 0 & 0 & \dfrac{\partial N_3}{\partial x} & 0 \\ 0 & 0 & \dfrac{\partial N_1}{\partial y} & 0 & 0 & \dfrac{\partial N_2}{\partial y} & 0 & 0 & \dfrac{\partial N_3}{\partial y} \\ 0 & \dfrac{\partial N_1}{\partial y} & \dfrac{\partial N_1}{\partial x} & 0 & \dfrac{\partial N_2}{\partial y} & \dfrac{\partial N_2}{\partial x} & 0 & \dfrac{\partial N_3}{\partial y} & \dfrac{\partial N_3}{\partial x} \end{bmatrix} \begin{bmatrix} w_1 \\ v_{x1} \\ \varphi_{y1} \\ w_2 \\ \varphi_{x2} \\ \varphi_{y2} \\ w_3 \\ \varphi_{x3} \\ \varphi_{y3} \end{bmatrix},$$

$k_b = B_b u_e$

and shear strain

$$\begin{bmatrix}\gamma_{xz}\\ \gamma_{yz}\end{bmatrix}=\begin{bmatrix}\mathrm{j}_x+\dfrac{\partial w}{\partial x}\\ \varphi_y+\dfrac{\partial w}{\partial y}\end{bmatrix}\quad\text{or}\quad\begin{bmatrix}\gamma_{xz}\\ \gamma_{yz}\end{bmatrix}=\begin{bmatrix}\dfrac{\partial N_1}{\partial x} & N_1 & 0 & \dfrac{\partial N_2}{\partial x} & N_2 & 0 & \dfrac{\partial N_3}{\partial x} & N_3 & 0\\ \dfrac{\partial N_1}{\partial y} & 0 & N_1 & \dfrac{\partial N_2}{\partial y} & 0 & N_2 & \dfrac{\partial N_3}{\partial y} & 0 & N_3\end{bmatrix}\begin{bmatrix}w_1\\ \varphi_{x1}\\ \varphi_{y1}\\ w_2\\ \varphi_{x2}\\ \varphi_{y2}\\ w_3\\ \varphi_{x3}\\ \varphi_{y3}\end{bmatrix};$$

$$\gamma = B_s\, u_e \tag{11}$$

2.2.2. Stiffness Matrix for Plate Bending

The stiffness matrix establishes the proportional relationship between applied nodal forces/moments and resulting nodal displacements/rotations. The virtual displacement field utilizes identical interpolation functions as the real displacement field, satisfying:

$$\underline{\overline{u}} = \underline{N}\,\underline{\overline{u}}_e \tag{12}$$

The virtual curvatures (k) and virtual shear strains (γ) derived from the virtual displacement field are:

$$\underline{\overline{k}} = \underline{B}_b\,\underline{\overline{u}}_e \quad \text{or} \quad \underline{\overline{k}}^T = \underline{\overline{u}}_e^T\,\underline{B}_b^T;$$

$$\underline{\overline{\gamma}} = \underline{B}_s\,\underline{\overline{u}}_e \quad \text{or} \quad \underline{\overline{\gamma}}^T = \underline{\overline{u}}^T\,\underline{B}_s^T.$$

The internal virtual work comprises two terms: the product of real bending moments and their corresponding virtual curvatures, plus the product of actual shear forces and associated virtual shear angles.

$$\begin{aligned}&\overline{W}_i = \int \underline{\overline{k}}^T\,\underline{m}\,dxdy + \int \underline{\overline{\gamma}}^T\,\underline{v}dxdy;\\ &\overline{W}_i = \int \underline{\overline{u}}_e^T\,\underline{B}_e^T\,\underline{D}_b\underline{B}_b\underline{u}_e dxdy + \int \underline{\overline{u}}_e^T\,\underline{B}_s^T\,\underline{D}_s\underline{B}_s\underline{u}_e dxdy;\\ &\overline{W}_i = \underline{\overline{u}}_e^T\,(\int \underline{B}_b^T\,\underline{D}_b\,\underline{B}_b dxdy + \int \underline{B}_s^T\,\underline{D}_s\,\underline{B}_s dxdy)\,\underline{u}_e.\end{aligned} \tag{13}$$

The virtual work done by external loads consists of force-displacement and moment-rotation products at all nodes:

$$\overline{W_a} = \overline{\underline{u}_e^T}\,\underline{F}_e. \tag{14}$$

The principle of virtual work is satisfied when the sum of internal virtual work equals external virtual work:

$$\begin{aligned}&\underline{\overline{u}}_e^T\,\left(\int \underline{B}_b^T\,\underline{D}_b\,\underline{B}_b\,dx\,dy + \int \underline{B}_s^T\,\underline{D}_s\,\underline{B}_s\,dx\,dy\right)\underline{u}_e = \underline{\overline{u}}_e^T\,\underline{F}_e;\\ &\left(\int \underline{B}_b^T\,\underline{D}_b\,\underline{B}_b\,dx\,dy + \int \underline{B}_s^T\,\underline{D}_s\,\underline{B}_s\,dx\,dy\right)\underline{u}_e = \underline{F}_e;\\ &\underline{K}_e^{\,b}\,\underline{u}_e = \underline{F}_e;\\ &\underline{K}_e^{\,b} = \int \underline{B}_b^T\,\underline{D}_b\,\underline{B}_b\,dx\,dy + \int \underline{B}_s^T\,\underline{D}_s\,\underline{B}_s\,dx\,dy.\\ &\text{(Bending)}\qquad\qquad\text{(Shear)}\end{aligned} \tag{15}$$

The plate element's stiffness matrix [K] comprises two distinct sub-matrices: a bending stiffness component and a shear stiffness component. As a conforming element, it maintains C^0 continuity across both displacement and rotation fields.

2.3. Mathematical Principle

Among existing analytical approaches, the layered finite element method (LFEM) with triangular formulation demonstrates high efficacy in evaluating the flexural behavior of RC slabs. The methods employs a stratified representation of plate elements, discretizing the cross-section into distinct concrete and steel layers, as illustrated conceptually in Figure 4 [5; 22; 23]. This layered approach facilitates accurate modeling of stress distributions across the RC slab using an assembly of plane stress elements.

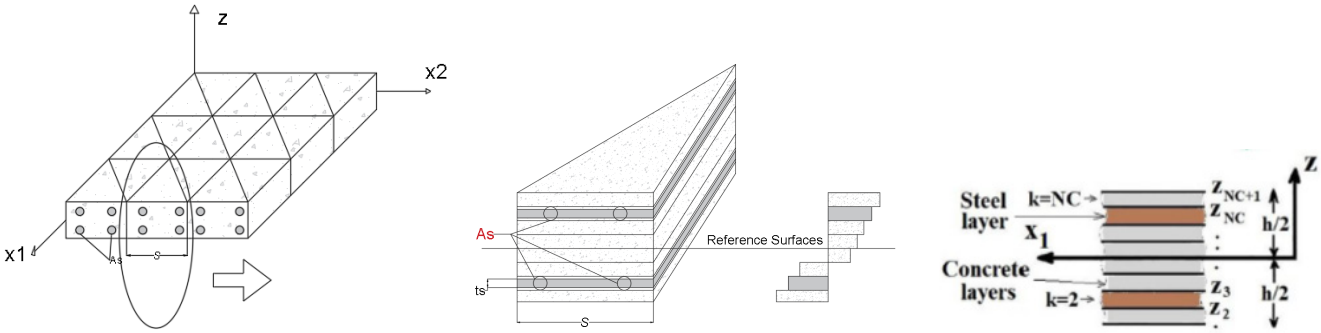

Figure 4. Typical triangular plate element for reinforced concrete plate structures

S o u r c e: made by D.A. Mawlood.

In this modeling approach, the RC slab is idealized as a composite system of perfectly bonded, uncracked concrete layers and equivalent steel layers. The reinforcement is represented using a smeared-layer approximation, with horizontal steel layers positioned at the centroidal levels of the actual reinforcement bars. The computational model employs the same number of smeared layers as physical reinforcement layers in the cross-section. Each equivalent steel layer is assigned uniaxial material properties corresponding to the orientation of the actual rebars. The equivalent thickness (t_s) of each steel layer is determined from the rebar cross-sectional area (A_s) and spacing (s) according to the relationship: $t_s = A_s / s$ [21].

Reddy's Third-Order Shear Deformation Theory (TSDT) overcomes the fundamental limitations of classical plate theories by eliminating both the normal hypothesis constraint and the requirement for planar cross-sections to remain plane after deformation [11]. The theory is founded on the following kinematic relations:

$$\begin{aligned} u(x,y,z) &= z\psi_x(x,y) + z^2\theta_x(x,y) + z^3\lambda_x(x,y); \\ v(x,y,z) &= z\psi_y(x,y) + z^2\theta_y(x,y) + z^3\lambda_y(x,y); \\ w(x,y) &= w_0(x,y). \end{aligned} \tag{16}$$

The kinematic functions ψ_x, ψ_y, θ_x, θ_y, λ_x, and λ_y represent undetermined parameters that characterize the cross-sectional warping deformation. Within the TSDT framework, these functions collectively introduce seven independent displacement variables. Specifically, the bending rotation components ψ_x and ψ_y describe the slope of the warped cross-section at the neutral plane $z = 0$, while the remaining variables account for higher-order deformation effects [11]. $\psi_x = \dfrac{\partial u}{\partial z}$, $\psi_y = \dfrac{\partial v}{\partial z}$, where $z = 0$.

The displacement field is mathematically represented by Equations (1) in the following form:

$$u(x,y,z) = z\psi_x(x,y) - \left(4z^3\right)/\left(3h^2\right)\left(\left(\psi_x(x,y) + \partial w_0(x,y)\right)/\partial x\right);$$

$$v\left(x,y,z\right) = z\,\psi_y\left(x,y\right) - \left(4z^3\right)/\left(3h^2\right)\left(\left(\psi_y(x,y) + \partial w_0(x,y)\right)/\partial y\right);$$

$$w(x,y) = w_0(x,y), \qquad (17)$$

where

$$\psi_x = -\frac{\partial w_0}{\partial x}, \psi_y = -\frac{\partial w_0}{\partial y}.$$

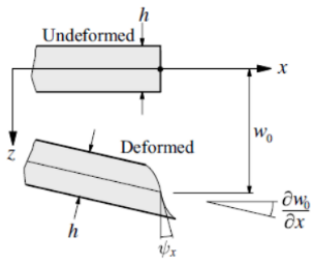

Figure 5. Unreformed and deformed plate segment

S o u r c e: made by C. Mittelstedt [11].

Consequently, Reddy's Third-Order Shear Deformation Theory incorporates just three degrees of freedom, as depicted in Figure 5.

2.4. Interconnections Between Layers

2.4.1. Strain Distribution Field

Based on the derived displacement-strain relationships, the strain components in the *i*-th layer of the RC slab can be determined [11], as illustrated in Figure 5.

$$\varepsilon_{xx} = \frac{\partial u}{\partial x} = z\frac{\partial \psi_x}{\partial x} - \frac{4z^3}{3h^2}\left(\frac{\partial \psi_x}{\partial x} + \frac{\partial^2 w_0}{\partial x^2}\right);$$

$$\varepsilon_{yy} = \frac{\partial u}{\partial y} = z\frac{\partial \psi_y}{\partial y} - \frac{4z^3}{3h^2}\left(\frac{\partial \psi_y}{\partial y} + \frac{\partial^2 w_0}{\partial y^2}\right);$$

$$\varepsilon_{zz} = \frac{\partial w}{\partial z} = 0;$$

$$\gamma_{yz} = \frac{\partial v}{\partial z} + \frac{\partial w}{\partial y} = \psi_y - \frac{4z^2}{h^2}\left(\psi_y + \frac{\partial w_0}{\partial y}\right) + \frac{\partial w_0}{\partial y};$$

$$\gamma_{xz} = \frac{\partial u}{\partial z} + \frac{\partial w}{\partial x} = \psi_x - \frac{4z^2}{h^2}\left(\psi_x + \frac{\partial w_0}{\partial x}\right) + \frac{\partial w_0}{\partial x};$$

$$\gamma_{xy} = \frac{\partial u}{\partial y} + \frac{\partial v}{\partial x} = z\left(\frac{\partial \psi_x}{\partial y} + \frac{\partial \psi_y}{\partial x}\right) - \frac{4z^3}{3h^2}\left(\frac{\partial \psi x}{\partial y} + \frac{\partial \psi_y}{\partial x} + 2\frac{\partial^2 w_0}{\partial x \partial y}\right).$$

These can be represented in vector form as:

$$\varepsilon^{(1)} = \begin{pmatrix} \varepsilon_{xx}^{(1)} \\ \varepsilon_{yy}^{(1)} \\ \gamma_{xy}^{(1)} \end{pmatrix} = \begin{pmatrix} \frac{\partial \psi_x}{\partial x} \\ \frac{\partial \psi_y}{\partial y} \\ \frac{\partial \psi_x}{\partial y} + \frac{\partial \psi_y}{\partial x} \end{pmatrix}; \; \varepsilon^{(3)} = \begin{pmatrix} \varepsilon_{xx}^{(3)} \\ \varepsilon_{yy}^{(3)} \\ \gamma_{xy}^{(3)} \end{pmatrix} = \begin{pmatrix} -\frac{4}{3h^2}\left(\frac{\partial \psi_x}{\partial x} + \frac{\partial^2 w_0}{\partial x^2}\right) \\ -\frac{4}{3h^2}\left(\frac{\partial \psi_y}{\partial y} + \frac{\partial^2 w_0}{\partial y^2}\right) \\ -\frac{4}{3h^2}\left(\frac{\partial \psi x}{\partial y} + \frac{\partial \psi_y}{\partial x} + 2\frac{\partial^2 w_0}{\partial x \partial y}\right) \end{pmatrix};$$

$$\gamma^{(0)}=\begin{pmatrix}\gamma_{yz}^{(0)}\\ \gamma_{xz}^{(0)}\end{pmatrix}=\begin{pmatrix}\psi_y+\dfrac{\partial w_0}{\partial y}\\ \psi_x+\dfrac{\partial w_0}{\partial x}\end{pmatrix};\quad \gamma^{(2)}=\begin{pmatrix}\gamma_{yz}^{(2)}\\ \gamma_{xz}^{(2)}\end{pmatrix}=\begin{pmatrix}-\dfrac{4}{h^2}\left(\psi_y+\dfrac{\partial w_0}{\partial y}\right)\\ -\dfrac{4}{h^2}\left(\psi_x+\dfrac{\partial w_0}{\partial x}\right)\end{pmatrix}.$$

The strain field can be expressed as follows:

$$\varepsilon=z\varepsilon^{(1)}+z^3\varepsilon^{(3)};$$
$$\gamma=\gamma^{(0)}+z^2\gamma^{(2)}. \tag{18}$$

2.4.2. Stress Fields in the Out-of-Plane Direction

The normal stress components are obtained from the strain field by applying Hooke's law, as given below: [6; 13]

$$\begin{bmatrix}\sigma_x\\ \sigma_y\\ \tau_{xy}\end{bmatrix}=\frac{E_i}{1-\mu^2}\begin{bmatrix}1 & \mu & 0\\ \mu & 1 & 0\\ 0 & 0 & \dfrac{1-\mu}{2}\end{bmatrix}\begin{bmatrix}\varepsilon_x\\ \varepsilon_y\\ \gamma_{xy}\end{bmatrix};$$

$$\sigma^i=\underline{D}^i\underline{\varepsilon}^i.$$

Using the strain definitions from Equation (18), the strains can be expressed as:

$$\sigma^i=\underline{D}^i\left(z\varepsilon^{(1)}+z^{(3)}\varepsilon^{(3)}\right). \tag{19}$$

The transverse shear stress components $\left(\tau_{xi},\tau_{yi}\right)$ for each layer in the reinforced concrete slab are determined using the following expressions:

$$\begin{bmatrix}\tau_{xz}\\ \tau_{yz}\end{bmatrix}=\frac{E_i}{2(1+\mu)}\begin{bmatrix}1 & 0\\ 0 & 1\end{bmatrix}\begin{bmatrix}\gamma_{xz}\\ \gamma_{yz}\end{bmatrix};$$

$$\tau^i=\underline{D}_s^i\gamma^i;$$
$$\tau^i=\underline{D}_s^i\left(\gamma^{(0)}+z^{(2)}\gamma^{(2)}\right), \tag{20}$$

where E_i represents the elastic modulus of the *i-th* layer in the reinforced concrete slab system, and μ denotes the Poisson's ratio characteristic of the reinforced concrete layers.

The layer-wise constitutive formulation accounts for material heterogeneity through distinct elastic modulus E_i, and Poisson's ratios μ for each layer i. The governing equations employ standard stress resultants obtained via thickness integration of stress components [24]:

$$M^0=\begin{pmatrix}M_{xx}^0\\ M_{yy}^0\\ M_{xy}^0\end{pmatrix}=\int_{-\frac{h}{2}}^{+\frac{h}{2}}\begin{pmatrix}\sigma_{xx}\\ \sigma_{yy}\\ \tau_{xy}\end{pmatrix}zdz;\qquad Q=\begin{pmatrix}Q_y\\ Q_x\end{pmatrix}=\int_{-\frac{h}{2}}^{+\frac{h}{2}}\begin{pmatrix}\tau_{yz}\\ \tau_{xz}\end{pmatrix}dz. \tag{21}$$

Here's a rigorous academic formulation of the additional force/moment resultants in TSDT:

$$P=\begin{pmatrix}P_{xx}\\P_{yy}\\P_{xy}\end{pmatrix}=\int_{-\frac{h}{2}}^{+\frac{h}{2}}\begin{pmatrix}\sigma_{xx}\\\sigma_{yy}\\\tau_{xy}\end{pmatrix}z^3 d\,;\qquad R=\begin{pmatrix}Ry\\Rx\end{pmatrix}=\int_{-\frac{h}{2}}^{+\frac{h}{2}}\begin{pmatrix}\tau_{yz}\\\tau_{xz}\end{pmatrix}z^2 dz\,. \tag{22}$$

2.4.3. Layer Interaction Mechanics in Reinforced Concrete Slabs

2.4.3.1. Layer of Steel Reinforcement

The reinforcing steel layers exhibit elastoplastic behavior, characterized by an idealized bilinear response. For the *i-th* reinforcement layer in the pre-yield regime, the constitutive [11] relationship is expressed as:

$$\sigma^i_{steel}=\underline{D}^i_{steel}\underline{\varepsilon}^i\quad,$$

where (ε^i) is represented by Equation 19. The sectional properties D_{steel} for steel;

$$\underline{D}^i_{steel}=\begin{bmatrix}E_s & 0 & 0\\0 & 0 & 0\\0 & 0 & 0\end{bmatrix}. \tag{23}$$

In Equation (23), E_s represents the elastic modulus of the *i-th* reinforcing steel layer. Upon yielding, the constitutive relationship transitions to a plastic regime, with the post-yield behavior described by the following incremental formulation:

$$\underline{D}^i_{steel}=\begin{bmatrix}E_{sp} & 0 & 0\\0 & 0 & 0\\0 & 0 & 0\end{bmatrix}.$$

The term E_{ps} refers to the plastic modulus of the steel layer after it has yielded [21].

2.4.3.2. Concrete Layer Properties

In its uncracked state, the concrete material exhibits isotropic, homogeneous linear elastic behavior. The constitutive relationship governing the *i-th* concrete layer's pre-cracking response is expressed as:

$$\sigma^i_{concrete}=\underline{D}^i_{concrete}\,\underline{\varepsilon}^i, \tag{24}$$

where (ε^i) is defined by Equation (18), and $D^i_{concrete}=\dfrac{E_i}{1-\mu^2}\begin{bmatrix}1 & \mu & 0\\\mu & 1 & 0\\0 & 0 & \dfrac{1-\mu}{2}\end{bmatrix}$.

The transverse shear stress components τ_{xz} and τ_{yz} in each concrete layer can be evaluated through application of the appropriate constitutive relationship:

$$\tau^i_{concrete}=\underline{D}^i_s\,\underline{\gamma}^i,\qquad D^i_s=\frac{E_i}{2(1+\mu)}\begin{bmatrix}1 & 0\\0 & 1\end{bmatrix}, \tag{25}$$

where E_i denotes the elastic modulus of the *i-th* concrete layer, and (μ) represents the Poisson's ratio characterizing the concrete material's transverse strain response.

When the principal stress state exceeds the concrete's tensile capacity (f_t), the elastic constitutive relations (Eqs. 24–25) no longer apply. This investigation adopts a smeared crack formulation [24] to model post-cracking concrete behavior. The smeared crack approach necessitates a material symmetry transition from isotropic to orthotropic behavior in the local coordinate frame (ξ, η, ζ). Here, the ξ-axis normal to the crack plane defines the material softening direction, while the η- and ζ-axes plane (aligned with principal stresses) maintains elastic stiffness. In the post-cracking phase, the constitutive relationship for the *i-th* concrete layer transforms to an orthotropic formulation in the local crack-aligned coordinate system (ξ, η, ζ), expressed as:

$$\begin{bmatrix} \sigma_\xi \\ s_\eta \\ \tau_{\xi\eta} \end{bmatrix} = \frac{E_i}{1-\mu^2} \begin{bmatrix} 1 & \mu & 0 \\ \mu & 1 & 0 \\ 0 & 0 & \rho\left(\frac{1-\mu}{2}\right) \end{bmatrix} . \begin{bmatrix} \varepsilon_\xi \\ \varepsilon_\eta \\ \gamma_{\xi\eta} \end{bmatrix}; \tag{26}$$

$$\begin{bmatrix} \tau_{\xi\zeta} \\ \tau_{\eta\zeta} \end{bmatrix} = \frac{E_i}{2(1+\mu)} \begin{bmatrix} 1 & 0 \\ 0 & \rho \end{bmatrix} \begin{bmatrix} \gamma_{\xi\zeta} \\ \gamma_{\eta\zeta} \end{bmatrix}. \tag{27}$$

Note that $(\rho \in (0.1])$ represents the shear retention factor, which is utilized to model the effects of aggregate interlock.

2.5. Mixed Element Stiffness Formulation

The element stiffness matrix components can be decomposed into membrane and bending contributions as follows:

$$K_{ei} = \sum_{i=1}^{L} K_{e,i}^m + K_{e,i}^b ; \tag{28}$$

$$\underline{K}_{e,i}^m = \iint \underline{t}\, \underline{B}_m^T\, \underline{D}_{m,i}\, \underline{B}_{m,i} dxdy ;$$

$$\underline{K}_{e,i}^b = \iint \underline{B}_{b,i}^T\, \underline{D}_{b,i}\, \underline{B}_{b,i} dxdy + \iint \underline{B}_{s,i}^T\, \underline{D}_{s,i}\, \underline{B}_{s,i} dxdy .$$

The stiffness contribution exhibits material-specific behavior: the steel reinforcement provides only membrane (in-plane) stiffness, while the concrete contributes to both membrane and bending (flexural) resistance.

$$K_{e,i}^m = K_{concrete}^m + K_{steel}^m = [K_{6,6}^m];$$

$$K_{e,i} = K_{e,i}^m + K_{e,i}^b = \begin{bmatrix} K_{6,6}^m & 0 \\ 0 & K_{9,9}^b \end{bmatrix}. \tag{29}$$

where $K_{6,6}^m$ and $K_{9,9}^b$ represent the membrane and bending stiffness matrices for the element, respectively.

2.6. Discretization of Finite Elements

The reinforced concrete slab is modeled using a three-node, triangular layered plate element that accounts for thickness effects. The development of this composite finite element requires discrete approximations of three key field quantities: (1) geometric configuration, (2) displacement fields, and (3) stress distributions. The proposed layered plate formulation incorporates 15 degrees of freedom (DOFs) per element, with the complete nodal configuration detailed in Figure 6.

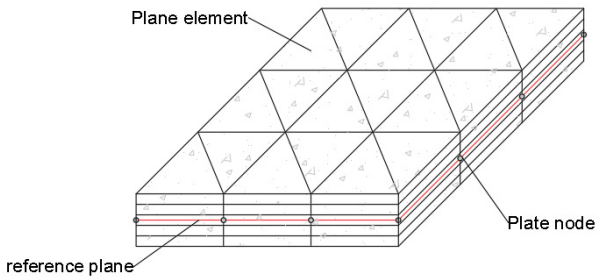

Figure 6. Meshing process of the RC slab using layered plate elements
S o u r c e: made by D.A. Mawlood.

2.7. Load Distribution Elements

The element loads are converted into equivalent nodal loads that yield identical external virtual work under virtual displacements as the original loads. This relationship is defined by Equations (10) and (15):

$$\underline{K}_e \, \underline{u}_e = \underline{F}_e \quad \text{or} \quad [K][d] = [P].$$

The reinforced concrete slab, subjected to element loads combining membrane and bending effects, can be expressed as:

$$\begin{bmatrix} K^m_{6,6} & 0 \\ 0 & K^b_{9,9} \end{bmatrix} \begin{bmatrix} d^m \\ d^b \end{bmatrix} = \begin{bmatrix} P^m \\ P^b \end{bmatrix},$$

where: d^m, d^b...membrane (u_1, u_2, u_3, v_1, v_2, v_3) and bending $(w_1, \varphi_{x1}, \varphi_{y1}, w_2, \varphi_{x2}, \varphi_{y2}, w_3, \varphi_{x3}, \varphi_{y3})$ element displacement; P^m, P^b .....membrane and bending element loads.

The nonlinear algebraic system is solved using a mixed-step iterative method that combines incremental loading with Newton — Raphson equilibrium iterations. Figures 7 and 8 illustrate how this approach applies loads incrementally while performing iterative corrections at each step to satisfy equilibrium conditions. Although the Newton-Raphson method improves solution accuracy, it requires additional computational effort.

The computational algorithm for the non-incremental Newton — Raphson method (Figure 8) executes the following sequence:

1. In the initialization phase, the structure is loaded with $\triangle P_1$, followed by computation of the first displacement approximation according to:

$$\bar{d}_0 = [\bar{K}_0(E_0)]^{-1} \triangle P_1, \tag{30}$$

where the global stiffness matrix is computed using the initial elastic modulus E_0.

2. From the computed displacements, element stresses σ (or strain ε) and updated moduli $E_i^{(N)}$ are determined. Equilibrium verification with the updated stiffness matrix yields residual forces:

$$\bar{r}_0 = \bar{K}_1(E_1)\bar{d}_0 - \triangle \bar{P}_1. \tag{31}$$

3. The residual forces induce corresponding corrective displacements:

$$\triangle \bar{d}_1 = [\bar{K}_1(E_1)]^{-1} \bar{r}_0. \tag{32}$$

4. The iterative correction process computes successive deflections $\bar{d}_1 = \bar{d}_0 + \triangle \bar{d}$, where each step generates residual forces $\bar{r}_2$ and displacement increments $\triangle \bar{d}_1$, until equilibrium is attained. The algorithm's general form is given by:

$$\begin{aligned} \overline{r}_j &= \overline{K}_{j+1}(E_{j+1})\overline{d}_j - \overline{P}; \\ \triangle\overline{d}_{j+1} &= [\overline{K}_{j+1}(E_{j+1})]^{-1}\overline{r}_j, \end{aligned} \quad \text{for} \quad j = 1,2,3... \tag{33}$$

The iterative process terminates when the residual forces diminish to a negligible magnitude. The total plate deflection is subsequently obtained through superposition of all incremental displacement components [5].

$$\overline{d} = \overline{d}_0 + \sum_{j=0}^{m} \triangle\overline{d}_{j+1} \, . \tag{34}$$

The described numerical procedure is successively applied to all load increments $\triangle P_1$ $(i = 1,2,...,n)$.

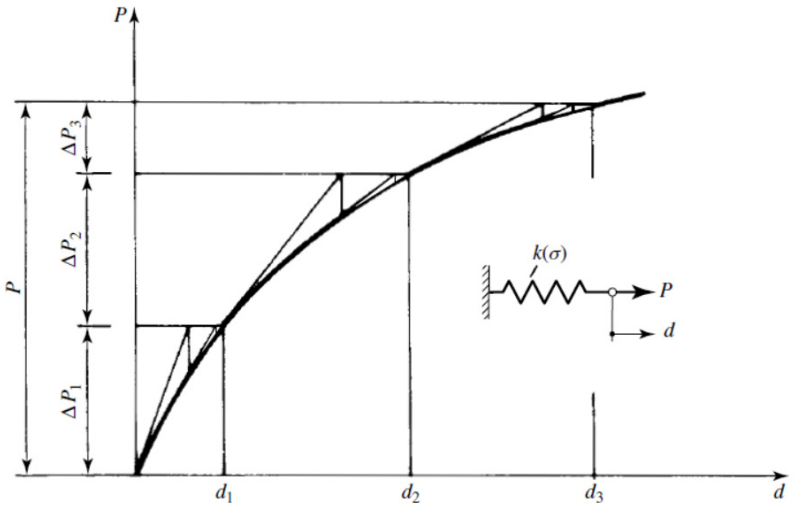

Figure 7. Step iteration or mixed procedure
S o u r c e: made by D.A. Mawlood.

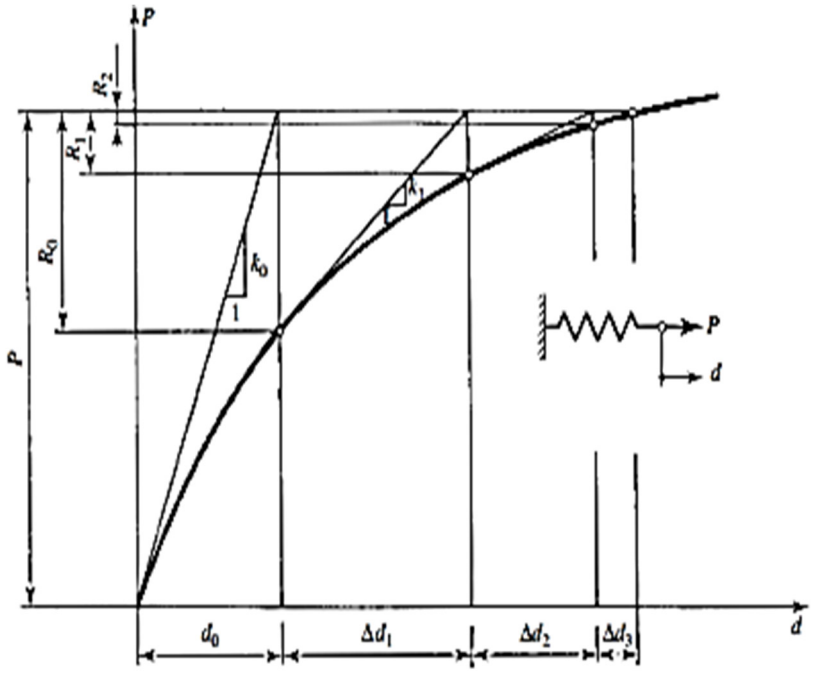

Figure 8. Iterative tangent stiffness procedure
S o u r c e: made by D.A. Mawlood.

3. Results and Discussion

This work presents a MATLAB implementation, based on the preceding theoretical framework, for nonlinear layer-wise finite element analysis specialized for triangular element formulations. To evaluate computational performance, the proposed method was applied to analyze three experimentally validated reinforced concrete slab specimens. All test cases had been previously characterized under controlled laboratory conditions, enabling direct comparison between numerical predictions and experimental results.

3.1. Analysis of One-Way Reinforced Concrete Slabs (S1)

A semi-precast one-way RC slab with dimensions 75 mm × 600 mm × 1650 mm was analyzed using the proposed layered finite element method with triangular elements. The slab incorporated mesh reinforcement consisting of 12 mm diameter steel bars spaced at 200 mm center-to-center, with a 25 mm concrete cover. Figure 9 illustrates the slab's geometric configuration, loading conditions, and boundary constraints.

The material properties were defined as follows: concrete with a modulus of elasticity of 26.420 GPa, Poisson's ratio of 0.15, and compressive strength of 31.6 MPa; steel reinforcement with an elastic modulus of 190 GPa, Poisson's ratio of 0.3, and yield stress of 535 MPa. This configuration replicates the experimental setup by Mohamed et al. [25], employing a two-point loading system with 516.7 mm spacing at mid span. The loading was applied through a hydraulic jack on a spread steel beam to create a pure bending region, with continuous load monitoring via a calibrated load cell. Strain gauges and LVDTs provided comprehensive deformation measurements through a high-frequency data acquisition system.

Taking advantage of symmetry, the finite element analysis modeled only half of the slab structure. Mesh convergence studies determined an optimal 3×4×2 grid of triangular laminated plate elements, with the thickness layered into six layers (five concrete layers and one equivalent steel layer). Figure 10 illustrates this configuration.

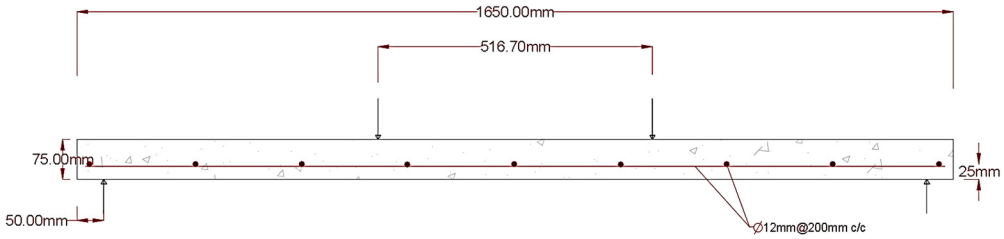

Figure 9. Schematic of the one-way RC slab: geometrical parameters, loading, and boundary conditions
S o u r c e: made by D.A. Mohamed et al. [25].

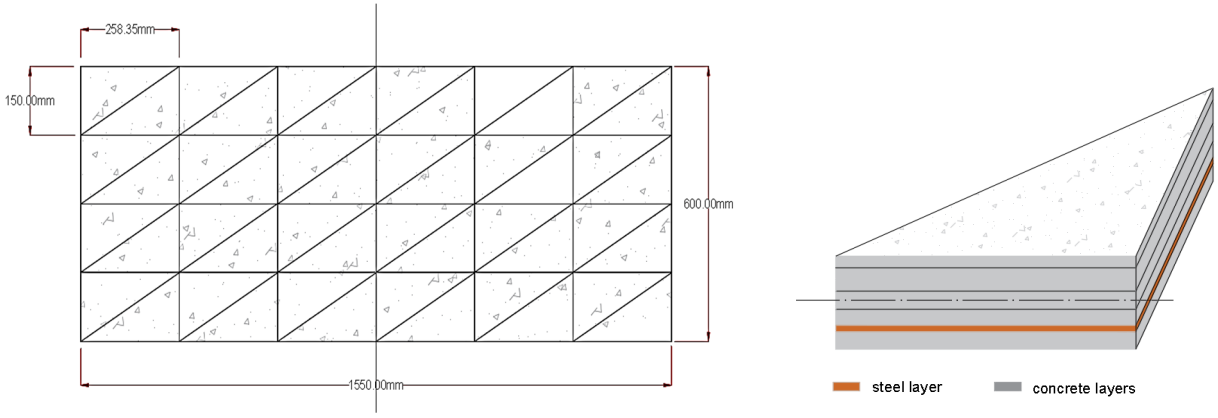

1 *2*

Figure 10. FE mesh of semi precast of reinforced concrete slab with toping concrete
1 — plan discretization; *2* — cross section discretization
S o u r c e: made by D.A. Mawlood.

Figures 11 and 12 compare the predicted load-deflection response with experimental data from Mohamed et al. and 3D ABAQUS simulations [25]. The proposed model demonstrates excellent agreement, showing a maximum deflection prediction error of 11.2% while maintaining a 99% correlation coefficient for the load-deflection relationship.

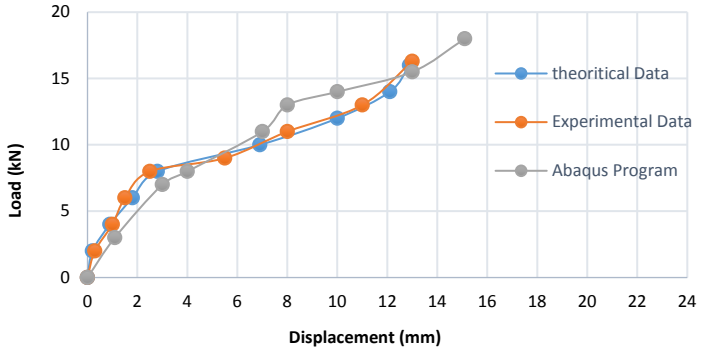

Figure 11. Load-deflection curve of the one-way RC slab at the mid-span
S o u r c e: made by D.A. Mawlood.

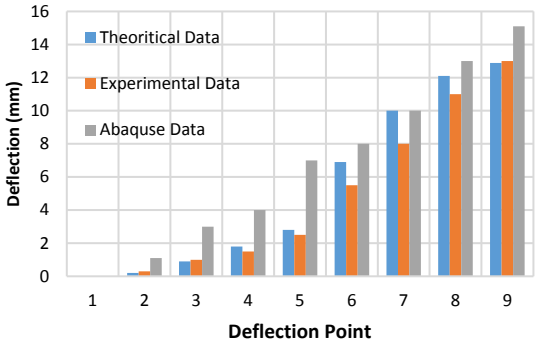

Figure 12. Deflection chat area
S o u r c e: made by D.A. Mawlood.

3.2. Two-Way Reinforced Concrete Slab with Single-Layer Reinforcement (S2)

The specimen had dimensions of 2.2 meters by 2.2 meters and a depth of 160 millimeters. All slabs had a loaded span of 2 meters in each direction, with a 0.1-meter overhang extending from the center of the supports on both sides. This study examines the two-way square reinforced concrete slab tested by Sara Nurmi et al. [26]. A point load is applied to the center of the slab, which is supported at all four corners. The tensile region of the reinforced concrete slab contains bidirectional steel reinforcement (x and y directions), with equal reinforcement ratios of $\rho_x = \rho_y = 0.23\%$. The mechanical properties of the slab are presented in Table 1, while Figure 13 depicts the geometric configuration and reinforcement arrangement. A central load was gradually applied to the slab using a hydraulic jack during testing, as conducted by Sara Nurmi et al. Deflections were measured at multiple locations, including the slab center, using LVDT sensors in Sara Nurmi's experimental setup [26].

Table 1

Material parameters of two-way slab with one layer of reinforcement

Material	Elastic modulus, MPa	Poisson's ratio	Yield stress, MPa	Compressive strength, MPa
Concrete	28,200	0.15		36
Steel	190,000	0.3	450	–

S o u r c e: made by D.A. Mawlood.

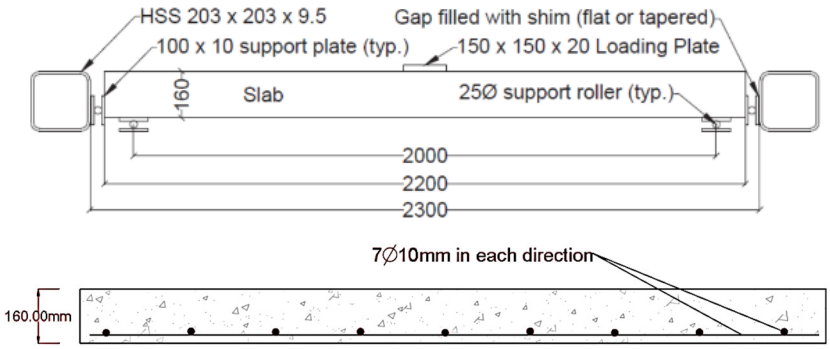

Figure 13. Geometrical parameters and reinforcement details of two way reinforced concrete slab
S o u r c e: made by Sara Nurmi's [26].

Figure 14 shows that the RC slab cross-section was discretized into five concrete layers, complemented by two equivalent steel layers representing reinforcement in orthogonal directions (x and y).

Figures 15 and 16 show the slab deflections computed using the proposed layered approach with triangular element discretization, along with the corresponding numerical results. For validation purposes, Figure 15 compares the model predictions with both experimental data from Nurmi et al. [26] and nonlinear finite element results obtained from Abaqus simulations. The comparative analysis demonstrates the effectiveness of the layered model in predicting deflection responses across the complete loading spectrum, from serviceability conditions to ultimate capacity.

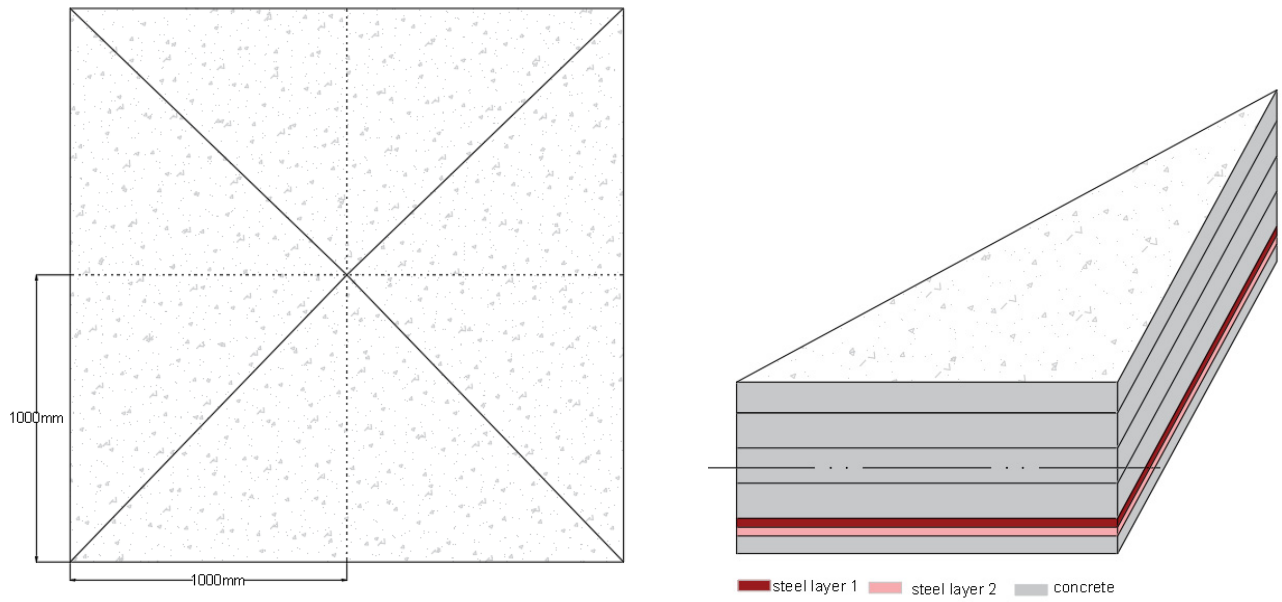

Figure 14. FE mesh of RC Slab: cross-section discretization

S o u r c e: made by D.A. Mawlood.

The benchmarking study reveals that the proposed layer method achieves superior accuracy in predicting two-way slab behavior compared to conventional Abaqus nonlinear solutions. The proposed model demonstrates excellent agreement, showing a maximum deflection prediction error of 2.59% while maintaining a 99.6% correlation coefficient for the load-deflection relationship.

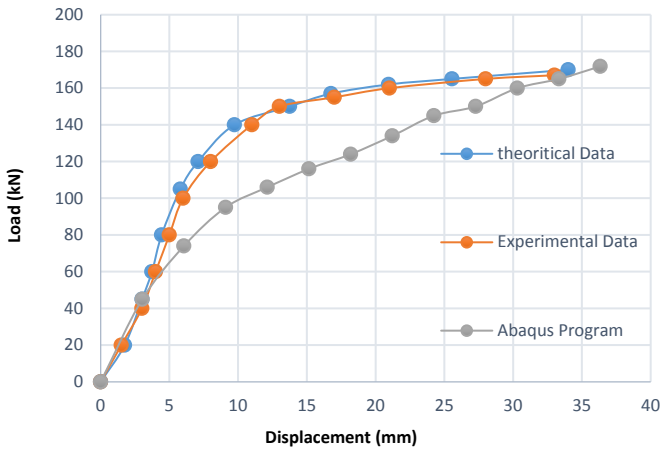

Figure 15. Load-deflection curve in the center of RC slab

S o u r c e: made by D.A. Mawlood.

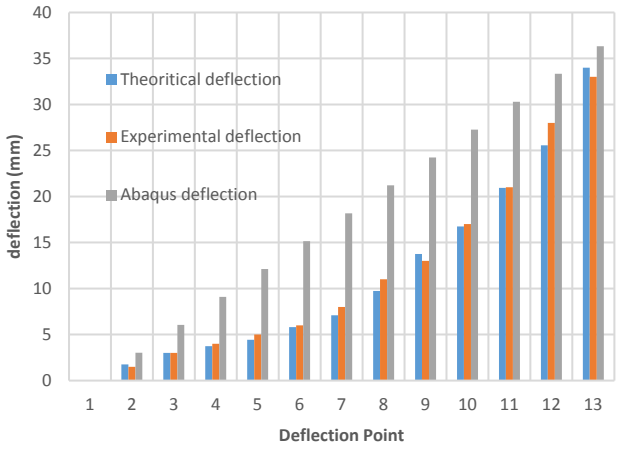

Figure 16. Deflections point

S o u r c e: made by D.A. Mawlood.

3.3. Two-Layer Reinforced Two-Way Concrete Slab (S3)

The experimental investigation conducted by Yao Xiao et al. examined a two-way RC slab system featuring dual reinforcement layers and full peripheral restraint. The test specimen comprised a 1200×1200×100 mm slab subjected to center-point loading. Key experimental parameters including material characteristics, are summarized in Table 2. The slab's reinforcement configuration consisted of orthogonal steel reinforcement distributed in both top and bottom layers, with detailed arrangement illustrated in Figure 17 [27].

Table 2

Material parameters of two-way reinforced concrete slab

Material	Elastic Modulus, MPa	Poisson's ratio	Longitude reinforcement diameter, mm	Yield stress, MPa	Compressive strength, MPa
Concrete	30,784	0.15	–	–	42.9
Steel	190,000	0.3	10	576	–

S o u r c e: made by D.A. Mawlood.

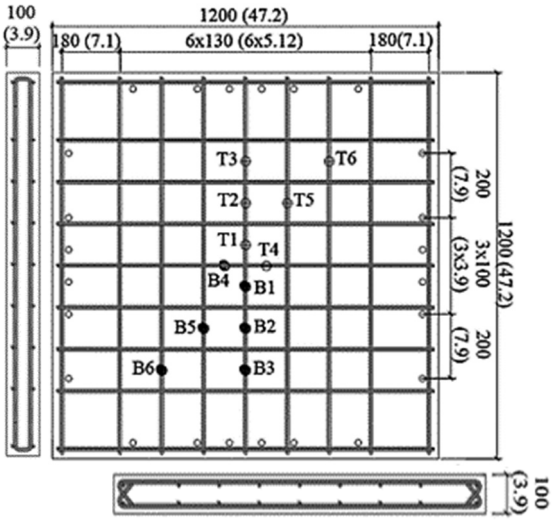

Clear cover (15 mm) and all reinforcement used diameter Φ10mm

Figure 17. Reinforced concrete slab details

S o u r c e: made by Yao Xiao et al. [27].

The two-way slab was reinforced with 10 mm diameter deformed steel bars (Grade 500) in orthogonal arrangements for both top and bottom layers, maintaining a uniform 15 mm concrete cover throughout. Figure 17 details the cross-sectional reinforcement layout and corresponding finite element discretization scheme. Figure 18 shows the load-deflection response at the slab center, capturing the complete nonlinear behavior from initial loading to ultimate capacity. This study presents the experimental results obtained by Yao Xiao et al., along with numerical results from nonlinear ABAQUS simulations and predictions from the triangular-shaped layer method. The load-deflection relationship predicted by the proposed methods shows excellent agreement with experimental observations. Compared to the nonlinear ABAQUS simulations, the triangular layer method demonstrates comparable accuracy in predicting both the ultimate load capacity and maximum deflection of the RC slab. The proposed model demonstrates a 7.32% error in maximum deflection prediction while maintaining a strong correlation coefficient of 99.6% between the predicted and experimental curves (Figures 19–20).

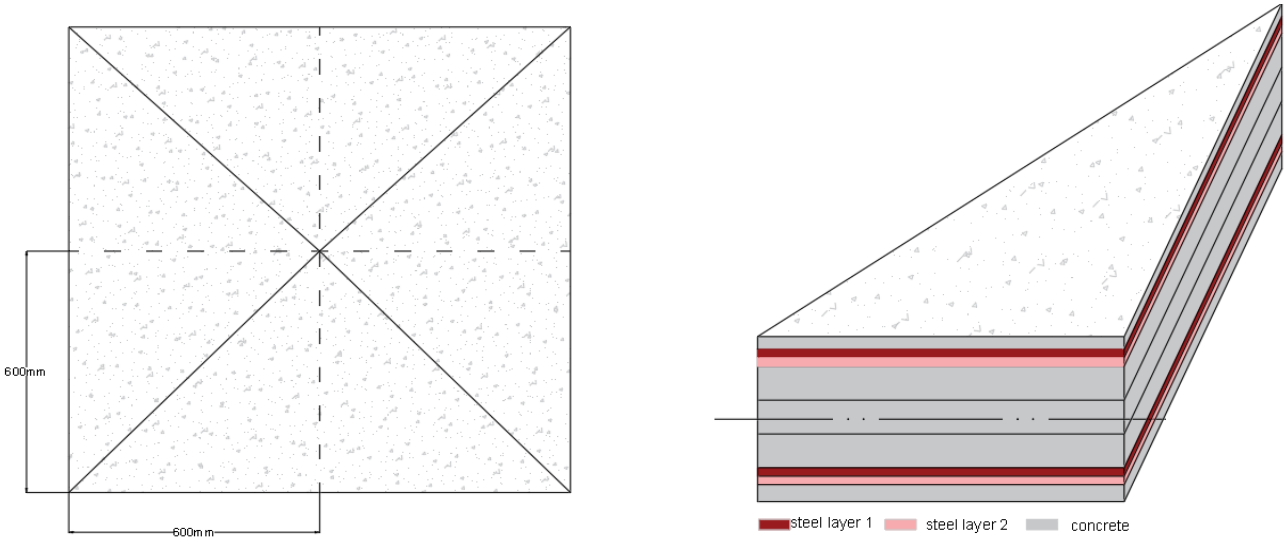

Figure 18. FE mesh of RC Slab: cross-section discretization

S o u r c e: made by D.A. Mawlood.

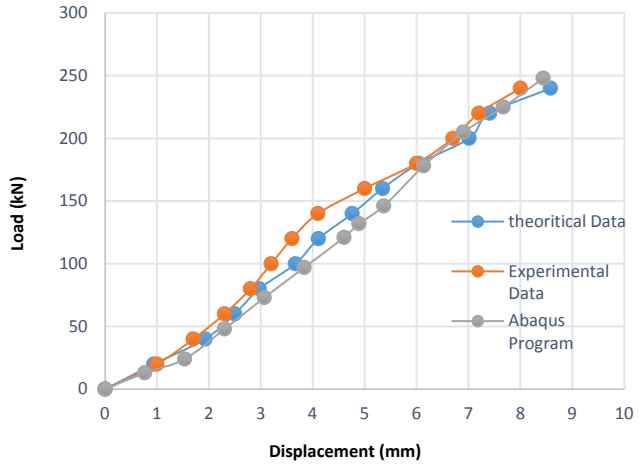

Figure 19. Load-deflection curve in the center of RC slab
S o u r c e: made by D.A. Mawlood.

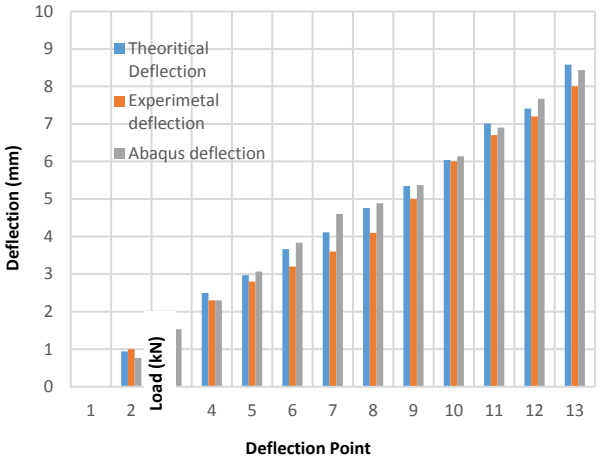

Figure 20. Deflection point
S o u r c e: made by D.A. Mawlood.

Figures 21–28 present the ABAQUS-simulated deflection patterns and stress distributions throughout the RC slab.

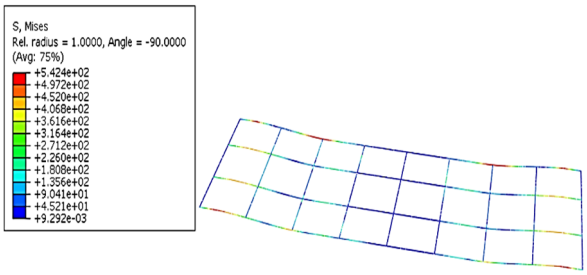

Figure 21. Stress in reinforced steel layer (S1)
S o u r c e: made by D.A. Mawlood.

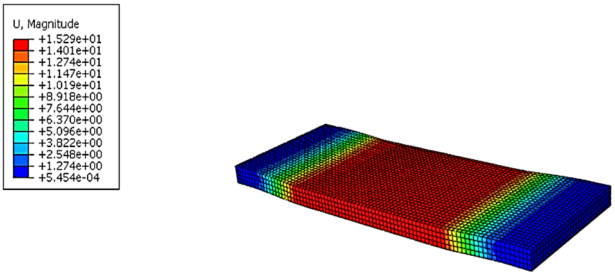

Figure 22. Deflection of concrete slab (S1)
S o u r c e: made by D.A. Mawlood.

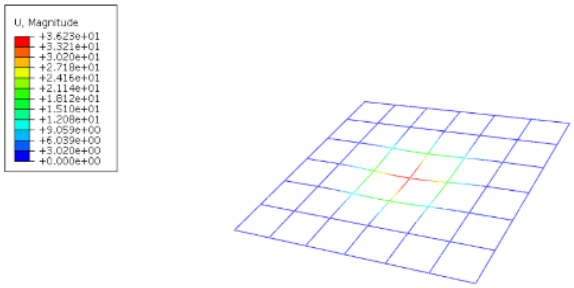

Figure 23. Effect of deflection on reinforced bars (S2)
S o u r c e: made by D.A. Mawlood.

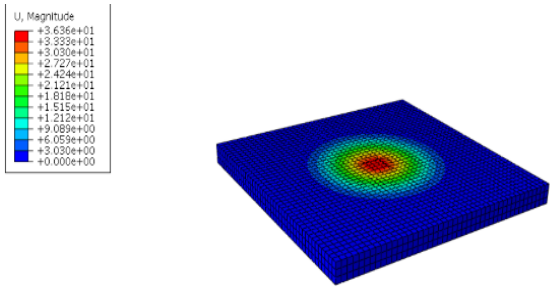

Figure 24. Effect of deflection on concrete slab (S2)
S o u r c e: made by D.A. Mawlood.

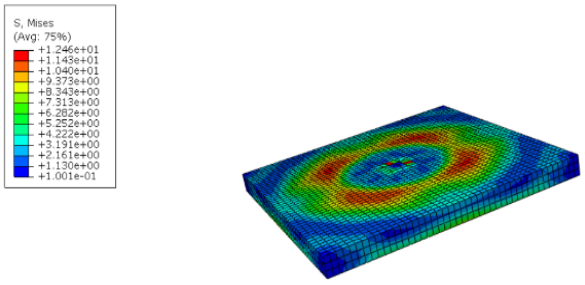

Figure 25. Effect of stress distribution on concrete slab (S2)
S o u r c e: made by D.A. Mawlood.

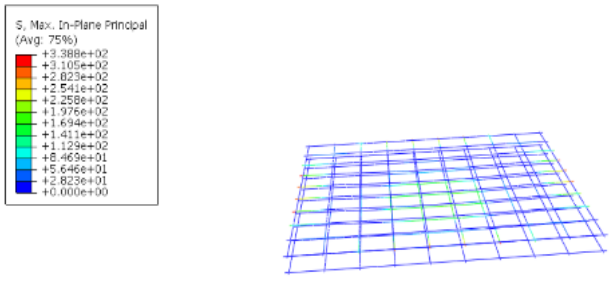

Figure 26. Stress in top and bottom reinforcement bars (S3)
S o u r c e: made by D.A. Mawlood.

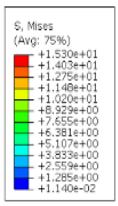

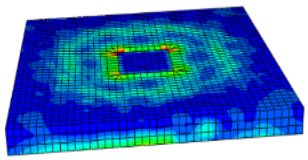

Figure 27. Stress in concrete slab (S3)
S o u r c e: made by D.A. Mawlood.

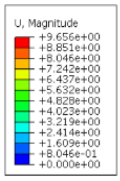

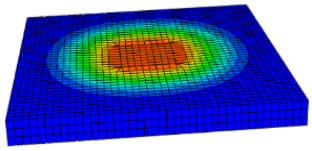

Figure 28. Deflection in concrete slab (S3)
S o u r c e: made by D.A. Mawlood.

4. Conclusion

1. The proposed triangular-layered finite element model enables direct computation of out-of-plane stress components in RC slabs, eliminating both the need for through-depth integration of equilibrium equations and the requirement for shear correction coefficients.

2. The proposed triangular-layered formulation maintains a constant number of unknown parameters for displacement and stress fields, independent of the number of layers, while preserving its layer-based framework.

3. The static nonlinear behavior of RC slabs up to failure was analyzed using a partial mixed stress-displacement variational principle combined with a three-noded triangular plate element.

4. The effectiveness of the proposed triangular-layered finite element model in predicting nonlinear structural responses was validated through comprehensive analyses of RC slabs with diverse geometries, reinforcement configurations, and boundary conditions.

5. Numerical results demonstrate that the proposed formulation accurately predicts both the ultimate load-carrying capacity and failure deflection of RC slabs.

6. Benchmark validation studies confirm the method's accuracy and computational efficiency, with ultimate deflection predictions exhibiting errors ranging from 2.59% (minimum) to 11.2% (maximum).

7. The proposed triangular-layered model accurately captures the complete load-deflection behavior of RC slabs while simultaneously predicting detailed structural responses, including deformation characteristics and stress component distributions.

8. The triangular-layered finite element model achieves an optimal balance between computational efficiency and predictive accuracy. Future work will extend this stress-displacement formulation to coupled material and geometric nonlinear analysis of reinforced concrete plate structures.

References

1. Le C.V., Ho V.Q., Ho P.L.H., Nguyen P.H. Limit state analysis of thin plates and slabs by a numerical pseudo-lower yield design approach. *Thin-Walled Structures*. 2022;172:108852. https://doi.org/10.1002/suco.202100532 EDN: BXJDTD

2. Issa M.S., Metwally I.M., Elzeiny S.M. Influence of fibers on flexural behavior and ductility of concrete beams reinforced with GFRP rebars. *Engineering Structures.* 2011;33:1754–1763. https://doi.org/10.1016/j.engstruct.2011.02.014

3. Amirkhani S., Lezgy Nazargah M. Nonlinear finite element analysis of reinforced concrete columns: Evaluation of different modeling approaches for considering stirrup confinement effects. *Structural Concrete*. 2022;23:2820–2836. https://doi.org/10.1002/suco.202100532 EDN: BXJDTD

4. Yeganeh-Salman A., Lezgy-Nazargah M. Evaluating the accuracy of mass scaling method in non-linear quasi-static finite element analysis of RC structures. *Structural Engineering and Mechanics*. 2023;85:485–500. https://doi.org/10.12989/SEM.2023.85.4.485

5. Szilard R. *Theories and applications of plate analysis: classical, numerical, and engineering methods*. Hoboken, NJ: John Wiley; 2004.

6. Werkle H. *Finite elements in structural analysis: Theoretical concepts and modeling procedures in statics and dynamics of structures*. Cham: Springer International Publ.; 2021. https://doi.org/10.1007/978-3-030-49840-5

7. Harmon T.G., Zhangyuan N. Shear strength of reinforced concrete plates and shells determined by finite element analysis using layered elements. *J Struct Eng.* 1989;115:1141–1157. https://doi.org/10.1061/(ASCE)0733-9445(1989)115:5(1141)

8. Polak M.A. Modeling punching shear of reinforced concrete slabs using layered finite elements. *SJ*. 1998;95(1): 71–80. https://doi.org/10.14359/528

9. Mahmood D., Rafiq S., Adbullah M. Nonlinear 3D Finite element model for square composite columns under various parameters. *Iraqi Journal of Civil Engineering.* 2022;16:19–28. https://doi.org/10.37650/ijce.2022.172882 EDN: NRXGDK

10. Mawlood D., Rafiq S. Nonlinear 3D Finite element model for round composite columns under various eccentricity loads. *Engineering and Technology Journal*. 2022;40:1605–1614. https://doi.org/10.30684/etj.2022.133106.1168 EDN: QTWLPF

11. Mittelstedt C. *Basics of elasticity theory. Theory of plates and shells*. Berlin, Heidelberg: Springer Berlin Heidelberg; 2023. p. 3–57. https://doi.org/10.1007/978-3-662-66805-4_1

12. Timošenko S.P., Woinowsky-Krieger S. *Theory of plates and shells*. 2nd. ed., [Nachdr.]. New York: McGraw-Hill; 1996.

13. Oñate E. *Structural analysis with the finite element method: linear statics.* Dordrecht London: Springer; 2009.

14. Jiang J., Mirza F.A. Nonlinear analysis of reinforced concrete slabs by a discrete finite element approach. *Computers & Structures.* 1997;65:585–592. https://doi.org/10.1016/S0045-7949(94)E0269-8

15. Saiah B., Bachene M., Guemana M., Chiker Y., Attaf B. On the free vibration behavior of nanocomposite laminated plates contained piece-wise functionally graded graphene-reinforced composite plies. *Engineering Structures*. 2022; 253:113784. https://doi.org/10.1016/j.engstruct.2021.113784 EDN: IKFKRC

16. Rodrigues Da Silva A., Paulo De Souza Rosa J. Nonlinear numerical analysis of prestressed concrete beams and slabs. *Engineering Structures*. 2020;223:111187. https://doi.org/10.1016/j.engstruct.2020.111187 EDN: AYEZIR

17. Van Vinh P., Avcar M., Belarbi M.-O., Tounsi A., Quang Huy L. A new higher-order mixed four-node quadrilateral finite element for static bending analysis of functionally graded plates. *Structures.* 2023;47:1595–1612. https://doi.org/10.1016/j.istruc.2022.11.113 EDN: GLXCXE

18. Cinefra M., Kumar S.K., Carrera E. MITC9 Shell elements based on RMVT and CUF for the analysis of laminated composite plates and shells. *Composite Structures*. 2019;209:383–90. https://doi.org/10.1016/j.compstruct.2018.10.039 EDN: WUDZCK

19. Moleiro F., Mota Soares C.M., Mota Soares C.A., Reddy J.N. A layerwise mixed least-squares finite element model for static analysis of multilayered composite plates. *Computers & Structures.* 2011;89:1730–1742. https://doi.org/10.1016/j.compstruc.2010.10.008

20. Liguori F.S., Corrado A., Bilotta A., Madeo A. A layer-wise plasticity-based approach for the analysis of reinforced concrete shell structures using a mixed finite element. *Engineering Structures*. 2023;285:116045. https://doi.org/10.1016/j.engstruct.2023.116045 EDN: XEVDXS

21. Wang R., Fang Z., Lezgy-Nazargah M., Khosravi H. Nonlinear analysis of reinforced concrete slabs using a quasi-3D mixed finite element formulation. *Engineering Structures.* 2023;294:116781. https://doi.org/10.1016/j.engstruct.2023.116781 EDN: HKKQXZ

22. Zhang Y.-G., Lu M.-W., Hwang K.-C. Finite element modeling of reinforced concrete structures. *Finite Elements in Analysis and Design.* 1994;18:51–8. https://doi.org/10.1016/0168-874X(94)90089-2

23. Zhang Y.X., Bradford M.A., Gilbert R.I. A new triangular layered plate element for the non-linear analysis of reinforced concrete slabs. *Commun Numer Meth Engng.* 2005;22:699–709. https://doi.org/10.1002/cnm.840

24. Willam K., Pramono E., Sture S. Fundamental issues of smeared crack models. In: Shah SP, Swartz SE, editors. *Fracture of Concrete and Rock.* New York, NY: Springer New York; 1989. p. 142–157. https://doi.org/10.1007/978-1-4612-3578-1_15

25. Mohamed M.S., Thamboo J.A., Jeyakaran T. Experimental and numerical assessment of the flexural behaviour of semi-precast-reinforced concrete slabs. *Advances in Structural Engineering.* 2020;23:1865–1879. https://doi.org/10.1177/1369433220904011 EDN: GDQHBJ

26. Nurmi S., Hoult N.A., Howell S.D. Distributed strain monitoring of two-way slabs. *Engineering Structures*. 2019;189:580–588. https://doi.org/10.1016/j.engstruct.2019.04.002

27. Xiao Y., Li B., Fujikake K. Experimental study of reinforced concrete slabs under different loading rates. *ACI Structural Journal.* 2016;113. https://doi.org/10.14359/51688067